

Evolution of the magnetic hyperfine field profiles in ion-irradiated Fe₆₀Al₄₀ film measured by nuclear resonant reflectivity

Andreeva, M.; Smekhova, A.; Baulin, R.; Repchenko, Y.; Bali, R.; Schmitz-Antoniak, C.; Wende, H.; Sergueev, I.; Schlage, K.; Wille, H. C.;

Originally published:

September 2021

Journal of Synchrotron Radiation 28(2021), 1535-1543

DOI: <https://doi.org/10.1107/S1600577521007694>

Perma-Link to Publication Repository of HZDR:

<https://www.hzdr.de/publications/Publ-32632>

Release of the secondary publication
on the basis of the German Copyright Law § 38 Section 4.

Evolution of the magnetic hyperfine field profiles in ion-irradiated Fe₆₀Al₄₀ film measured by nuclear resonant reflectivity

M. A. Andreeva¹, A. Smekhova^{2,3}, R. A. Baulin^{1,4}, Yu. L. Repchenko⁴, R. Bali⁵, C. Schmitz-Antoniak⁶, H. Wende⁶, I. Sergueev⁷, K. Schlage⁷ and H.-C. Wille⁷

¹ Faculty of Physics, M. V. Lomonosov Moscow State University, Moscow 119991, Russian Federation

² Peter-Grünberg-Institute (PGI-6), Jülich Research Center, 52425 Jülich, Germany

³ Helmholtz-Zentrum Berlin für Materialien und Energie (HZB), D-12489 Berlin, Germany

⁴ National Research Centre 'Kurchatov Institute', Pl. Kurchatova 1, Moscow 123182, Russian Federation

⁵ Helmholtz-Zentrum Dresden-Rossendorf, Bautzner Landstr. 400, 01328 Dresden, Germany

⁶ Faculty of Physics and Center for Nanointegration Duisburg-Essen (CENIDE), University of Duisburg-Essen, D-47048 Duisburg, Germany

⁷ Deutsches Elektronen-Synchrotron DESY, 22607 Hamburg, Germany

*Correspondence e-mail: mandreeva1@yandex.ru

Keywords: Magnetic patterning, ion irradiation, x-ray reflectivity, hyperfine interactions, nuclear resonant scattering, magnetic depth-profiles, Mössbauer spectroscopy.

Abstract

Nuclear resonant reflectivity (NRR) from an Fe₆₀Al₄₀ film was measured using synchrotron radiation at several grazing angles near the critical angle of the total external reflection. By laterally resolved measurements after 20 keV Ne⁺ ion irradiation with gradually varied fluences of 0 - 3.0×10¹⁴ ions/cm², the progressive creation of the ferromagnetic A2 phase with increasing ion fluence was confirmed. The observed depth-selectivity of the method has been explained by application of the standing wave approach. From the time spectra of the nuclear resonant scattering in forward or diffraction directions the depth-profiles for different hyperfine fields were extracted. The results evidence that the highest magnetic hyperfine fields (~ 18 ÷ 23 T) are initially created at the center part of the film and partially at the bottom interface with SiO₂ substrate. The evolution of the ferromagnetic onset, commencing at a fixed depth within the film and propagating towards the interfaces has been directly observed. At higher fluence (3.0×10¹⁴ ions/cm²) the depth distribution of the ferromagnetic fractions became more homogeneous across the film depth in accordance with previous results.

1. Introduction

The ability to control magnetic properties spatially at the nanoscale, can be useful for devices requiring magnetic modulations, such as data storage media. Modulation of the saturation magnetization can be achieved in selected materials where atomic displacements lead to drastic changes of magnetic behavior. A prototype material is the Fe₆₀Al₄₀ alloy, which is known to be paramagnetic in its B2 ordered state (Huffman & Fisher, 1967; Beck, 1971) Disorder caused by site-swapping between the Fe and Al atoms invokes an increase of the Fe-Fe nearest neighbor interaction along with an increase of the lattice parameter, leading to the onset

of ferromagnetism. The disordered Fe₆₀Al₄₀ phase is of the A2 structure, and this B2 to A2 transition can be induced by the irradiation of energetic ions (Fassbender *et al.*, 2008; Menéndez *et al.*, 2009; Bali *et al.*, 2014) as well as laser pulses (Ehrler *et al.*, 2018). Recently it has been shown that paramagnetic → ferromagnetic phase transformation can also be reversible in similar other alloys such as B2 Fe₅₀Rh₅₀ (Merkel *et al.*, 2020). Thus, magnetic properties can be modulated in alloy thin films by modification of lattice disorder, realized with industrially relevant ion- accelerators.

In the case of ion-irradiation, energetic ions penetrate into the B2 Fe₆₀Al₄₀ lattice, generating vacancies, that recombine with thermally diffusing atoms; since the recombination process is stochastic, site-swapping between the Fe and Al atoms occurs. The antisite defects thus formed are correlated with the ferromagnetic onset (Ehrler *et al.*, 2020). Since the depth penetration of ions in matter follows a quasi-Gaussian profile, and the penetration depth can be controlled via the ion-energy, it is possible to exert a degree of control on the depth-distribution of the magnetization (Röder *et al.*, 2015).

Irradiation of B2 Fe₆₀Al₄₀ thin films with light noble gas ions, such as Ne⁺, has been deployed to manipulate magnetic domains (Tahir *et al.*, 2015a). The investigation was performed by using longitudinal magneto-optical Kerr effect (L-MOKE) with magnetic domains imaging. The dynamic behavior of the Ne⁺ irradiated Fe₆₀Al₄₀ thin films has been investigated by ferromagnetic resonance (Tahir *et al.*, 2015b; Schneider *et al.*, 2019). It was shown that the observed spin-wave modes are directly related to the effective ferromagnetic thickness which increases with increasing the ion energy, as increasing ion-energy leads to its deeper penetration. Röder *et al.* (2015) investigated Fe₆₀Al₄₀ thin films irradiated by Ne⁺ ion of different energies using electron holography in TEM. The depth and lateral distribution of the magnetized regions at the nanoscale were observed by magnetic flux lines which became apparent via the phase shift of the scattered electrons. By means of X-ray magnetic circular dichroism (XMCD) and analysis of the extended X-ray absorption fine structure (EXAFS) measurements, performed at ID12 beamline of the European Synchrotron (ESRF), it has been shown that an increase of the irradiation fluence provided a progressive rise of the Fe magnetic moment revealing the occurring change of the chemical disorder in the Fe₆₀Al₄₀ alloy (La Torre, *et al.*, 2018). Recent XMCD results obtained with soft X-rays at the Helmholtz-Zentrum Berlin (HZB) have confirmed these findings (Smekhova *et al.*, submitted).

In preceding works the main attention was paid to the saturation magnetization of the whole film as well as to the penetration depth of the Ne⁺ ions and to the corresponding effective thickness of the created ferromagnetic layer. A possible decrease of ferromagnetic order near the surface caused by oxidation has already been discussed (Röder *et al.*, 2015), but the interpretation needs independent verification. At this point, X-ray methods can provide more detailed information about the magnetic structure of irradiated films. X-ray reflectometry possesses a sub-nanometer depth resolution for the electronic density shaping (Segmüller, 1973; Liu *et al.*, 2013; Macke *et al.*, 2014), and this technique complemented with resonant scattering near absorption edges or with nuclear resonant excitation opens a way for a detailed characterization

of magnetization depth profiles (see e.g. Ishimatsu *et al.* 1999, Jaouen *et al.*, 2004; Gibert *et al.*, 2016; Schlage *et al.*, 2009; Andreeva *et al.*, 2015; Andreeva *et al.*, 2018; Khanderao *et al.*, 2020).

In this work we have used the nuclear resonant reflectivity (NRR) technique with synchrotron radiation (SR) in order to get the depth distribution of hyperfine fields on ^{57}Fe nuclei in the $\text{Fe}_{60}\text{Al}_{40}$ film affected by 20 keV Ne^+ ions with different fluences from 0 to 3.0×10^{14} ions/cm² fluence gradually varied along a film surface. In this way, we track the gradual increase of the saturation magnetization caused by the atomic displacements. NRR can be performed for the fully ordered structure at 0 approaching the disordered structure for the highest fluence considered in this study. Consequently, the depth picture of the magnetic phase formation has been obtained under the sequentially increasing irradiation fluence.

2. Experimental

The $\text{Fe}_{60}\text{Al}_{40}$ thin film of ~ 40 nm thickness was prepared by magnetron sputtering on $\text{SiO}_2(150 \text{ nm})/\text{Si}(001)$ substrate with further annealing in vacuum at 773 K for 1 hr. to obtain the B2 ordered structure. B2 ordering is indicated by the occurrence of the 100 superstructure reflections (Bali *et al.*, 2014; Ehrler *et al.*, 2020; Smekhova *et al.*, submitted). For the present experiment the sample had the size of $\sim 5 \times 10$ mm. 20 keV Ne^+ irradiation had been undertaken with a gradual increasing fluence from 0 to 3.0×10^{14} ions/cm² along the sample surface with the help of a shutter *in situ* moved in steps of ~ 0.1 mm (in total 30 steps). In such a way the “disorder-gradient” sample was made (Fig. 1). It should be marked that the sample was not enriched by ^{57}Fe (the natural abundance is 2.14(1)%), so the preliminary NRR measurements had been done which proved the possibility of NRR measurements with such $\text{Fe}_{60}\text{Al}_{40}$ films.

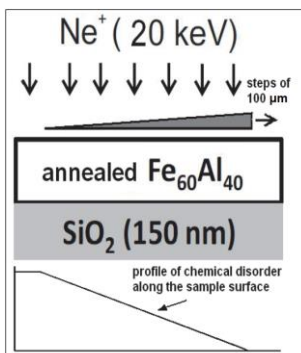


Figure 1

Schematic picture of the sample studied.

The measurements were done at the Dynamics beamline P01 of the PETRA III, DESY (Deutsches Elektronen-Synchrotron, Hamburg) using nuclear resonant scattering with ^{57}Fe Mossbauer transition at 14.4 keV. During measurements, the synchrotron was operated in the 40 bunch mode with a bunch separation of 192 ns. The transverse size of the beam on the sample surface was only ~ 0.16 mm which allowed laterally selected measurements. In spite of the natural abundance of ^{57}Fe (2.14 %) in the sample it became possible to get the NRR time spectra

at several grazing angles in vicinity of the critical angle with reasonable statistics. All measurements were performed at room temperature.

Nuclear resonant (Mössbauer) scattering with synchrotron radiation at the P01 beamline is basically measured in the time domain by detecting the delayed response after prompt pulse of the synchrotron beam. That is possible due to the relatively long lifetime of the excited resonant level (141 ns for ^{57}Fe isotope). In contrast to Mössbauer spectroscopy the hyperfine splitting of the nuclear levels appears in the time evolution of the delayed response as quantum beats (see e.g. Trammell & Hannon, 1978; Ruffer *et al.*, 1991; Smirnov, 1999). The period of oscillations Δt is connected with the energy difference of the interfering resonant lines ΔE by the simple expression $\Delta E = h / \Delta t$ (h is the Planck constant). A rather fast oscillations in the NRR time spectra are a direct evidence of the appearance of the magnetic ordering. The X-ray reflectivity was measured beforehand the NRR measurements as the prompt response.

3. Results and discussion

X-ray reflectivity curves were measured for resonant wavelength of 0.086 nm at different positions of the sample (Fig. 2). Each curve contains ~ 19 Kiessig fringes in the angular range from 0 up to 0.021 rad directly determining film thickness (Segmüller, 1973).

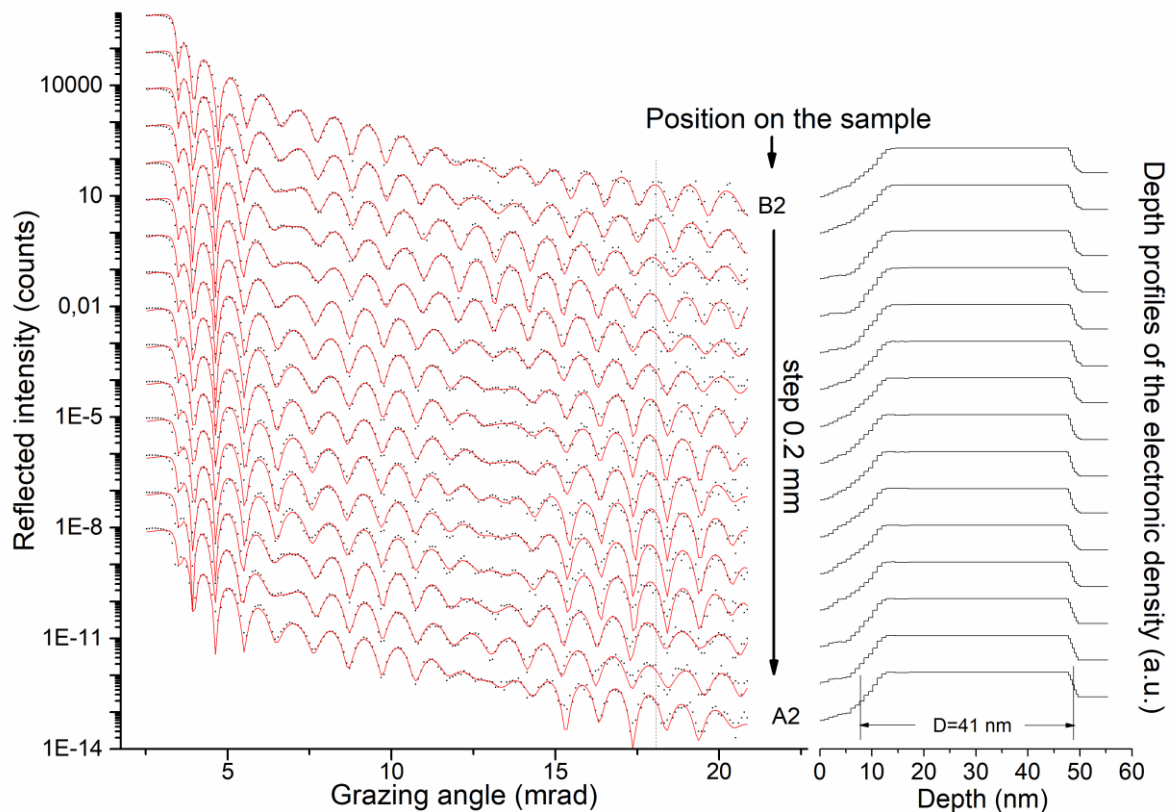


Figure 2

X-ray reflectivity curves for 14.4 keV radiation measured at 15 different positions on the gradient $\text{Fe}_{60}\text{Al}_{40}$ film (left side, dots are the experimental data, solid lines are the fit) and the results of their fit (right side), giving the depth-profiles of the X-ray refraction $|\delta|$, proportional to the electronic density. All curves are vertically shifted. The dashed vertical line is drawn in

order to clarify the small change of the oscillation frequency, corresponding to the increase of the film thickness caused by the ion irradiation.

Very small increase of the film thickness (~ 0.5 nm) due to the irradiation was revealed by change of the oscillation frequency. The result corresponds to the $\sim 1\%$ increase of the lattice parameter determined by X-ray diffraction (Liedke *et al.*, 2015; Ehrler *et al.*, 2020; La Torre, *et al.*, 2018). The peculiarities of the oscillation shapes characterize the top and bottom interfaces. Quite good fit of their remarkable variations specifies a tiny change of the top defective layer of ~ 10 nm thickness by the different irradiation fluence (Fig. 3). The defect containing thickness includes the surface oxide layer.

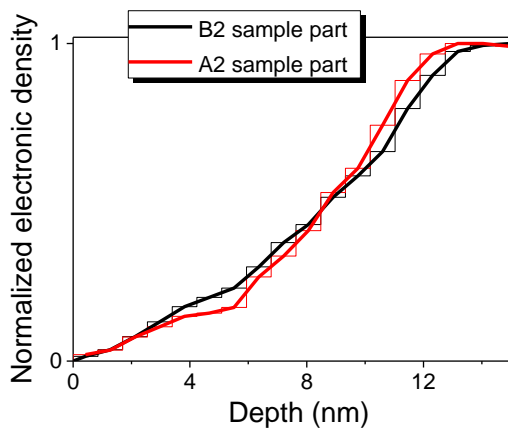


Figure 3

Scaled-up part of the electronic density for two ends of the film, obtained from X-ray reflectivity curves, demonstrating the change of the top defective layer under the ion irradiation.

The NRR time spectra were measured at several grazing angles near the critical angle of the total external reflection. The external field B^{ext} of 0.13 T was applied parallel or perpendicular to the SR beam in the surface plane supposed to be high enough in order to fully magnetize the sample and arrange magnetic hyperfine fields along the external field. Magnetically split resonant spectra with relatively large ΔE give the fast, recognizable oscillation pattern in the NRR time spectra, therefore the appearance of the quantum beats oscillations indicates the progressive creation of the ferromagnetic A2 phase in the $\text{Fe}_{60}\text{Al}_{40}$ film with increasing ion fluence (Fig. 4).

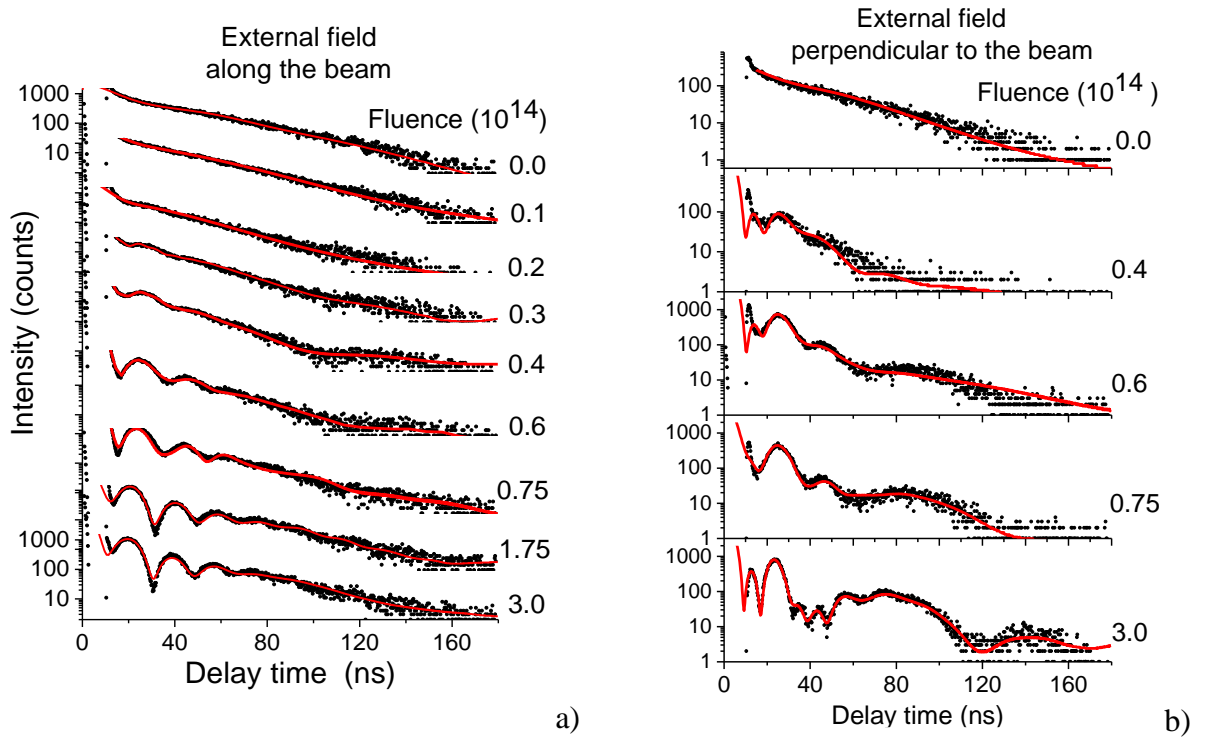


Figure 4

NRR time spectra measured at the critical angle of the total external reflection and at different positions of the SR beam on the gradually irradiated sample. The external magnetic field B^{ext} was applied either parallel to the SR beam direction (a) or perpendicular (b). Symbols are the experimental counts, lines are the fit.

The treatment of the NRR time spectra was performed on the basis of the matrix theory of reflectivity from anisotropic multilayers (Borzdov, 1976; Azzam & Bashara, 1977). In this theory the propagation of radiation in the reflecting stratified media is described by the 4×4 propagation matrix, characterizing the evolution of the 4 tangential components of the electric and magnetic field of radiation $\{H_x(z), H_y(z), -E_y(z), E_x(z)\}$ along depth z . In the case of the grazing angles θ the propagation matrix is represented by the expression (Andreeva, 1986a; Andreeva, 1986b):

$$\hat{M} \equiv \begin{pmatrix} 0 & 0 & 1 & 0 \\ \hat{\chi}_{xz} & 0 & 0 & \sin^2\theta + \hat{\chi}_{xx} \\ \sin^2\theta + \hat{\chi}_{zz} & 0 & 0 & \hat{\chi}_{zx} \\ 0 & 1 & 0 & 0 \end{pmatrix} \quad (1)$$

The susceptibility tensor $\hat{\chi}$ of the Mössbauer medium consists from two parts associated with the scattering by the electrons χ^{el} and by resonant nuclei $\hat{\chi}^{nucl}(\omega)$:

$$\hat{\chi} = \chi^{el} + \hat{\chi}^{nucl}(\omega), \quad (2)$$

The electronic part of susceptibility is a scalar function of z (apart from the absorption edges)

$$\chi^{el}(z) = -\frac{\lambda^2}{\pi} \rho(z) r_0 (Z + \Delta f' - i\Delta f''), \quad (3)$$

where $\rho(z)$ is a volume density of atoms, r_0 is the classical electron radius, Z is atomic number, $\Delta f'$ and $\Delta f''$ are the anomalous dispersion corrections for the scattering amplitude. It does not depend on the energy in the very narrow frequency range of the Mössbauer scattering, though it essentially influences the Mössbauer reflectivity spectra in the energy and time domains. Therefore, the fit of the X-ray reflectivity curve for each beam position had been done before fitting the corresponding NRR time spectra. The nuclear part of susceptibility $\hat{\chi}^{nucl}(\omega, z)$ is presented by the expression (Trammell, 1962; supplement to Andreeva *et al.*, 2015):

$$\begin{aligned} \hat{\chi}^{nucl}(\omega, z) = \\ = -A^{\alpha Fe} \sum_j C_j(z) \sum_{m_e, m_g} \frac{\left| \langle I_g m_g L \Delta m | I_e m_e \rangle \right|^2}{\hbar \omega - E_{jR}(m_e, m_g) + \frac{i\Gamma_j}{2}} \vec{h}_{\Delta m, j} \circ \vec{h}_{\Delta m, j}^*, \end{aligned} \quad (4)$$

where m_e, m_g are the magnetic quantum numbers of the ground and excited levels, j numerates the kind of the hyperfine field (multiplet number in a Mössbauer spectrum), $E_{jR}(m_e, m_g)$ are the hyperfine transition energies, which are determined for each multiplet by common Mössbauer parameters such as an isomer shift δ_j (or central shift CS), magnetic hyperfine field \mathbf{B}_j^{hf} and quadrupole splitting ΔE_j^Q , Γ_j are the full width of the resonant level, $\langle I_g m_g L \Delta m | I_e m_e \rangle$ are the Clebsch–Gordan coefficients, $\hat{h}_{\Delta m, j}$ in (4) are the spherical unit vectors (orts) of the hyperfine field principal axis, $\Delta m = m_e - m_g = \pm 1, 0$ for M1 transition.

The outer product of these unit vectors $\vec{h}_{\Delta m} \circ \vec{h}_{\Delta m}^*$ determines the tensor properties of the nuclear resonance susceptibility. $A^{\alpha Fe}$ is a constant which includes different parameters of the nuclear 14.4 keV transition in ^{57}Fe :

$$A^{\alpha Fe} = -\frac{\lambda}{2\pi} \frac{\Gamma_{nat}}{2} \sigma_{res} \frac{2L+1}{2I_e+1} \rho^{\alpha Fe} Q^{enrich} f^{LM} \cong -7.19 \times 10^{-6} \text{ mm/s}, \quad (5)$$

where $L=1$, $I_e=3/2$, $I_g=1/2$, $\sigma_{res}=2.56 \cdot 10^{-4} \text{ nm}^2$ is the resonant cross-section, $\lambda=0.086 \text{ nm}$, $\Gamma_{nat}=0.097 \text{ mm/s}$ (4.665 neV), f^{LM} is the Lamb–Mössbauer factor which is ~ 0.7 in $\alpha\text{-Fe}$ at room temperature, $Q^{enrich}=0.95$ is the ideal ^{57}Fe isotope enrichment, $\rho^{\alpha Fe}=84.9 \text{ nm}^{-3}$ is the volume density of the iron atoms in $\alpha\text{-Fe}$. In our case $Q^{enrich}=0.0214$ and volume density of iron atoms in $\text{Fe}_{60}\text{Al}_{40}$ differs from the density in $\alpha\text{-Fe}$. That essentially decreases $\hat{\chi}^{nucl}$. In calculations the real parameters of the nuclear resonant scattering are taken into account by a proper normalization of the coefficients $C_j(z)$.

The dimensionless coefficients $C_j(z)$ in (4) are the “weight” of the j -multiplet in the total susceptibility, which takes into account the relative volume density of the resonant nuclei possessing j type of hyperfine splitting, the given ^{57}Fe enrichment, the possible difference of f_j^{LM} from the accepted value of 0.7 due to the different environments or another temperature. Fitting the depth profiles $C_j(z)$ is the basic task for the interpretation of the NRR spectra along with determinations of the Mössbauer parameters \mathbf{B}_j^{hf} , ΔE_j^Q , δ_j and orientation of the $\hat{h}_{\Delta m, j}$ at each position of the gradient sample. For the model calculations and for a fit of the experimental NRR spectra the program pack “REFTIM” has been used (Andreeva, 2008). The fitting result for the NRR time spectra measured at several grazing angles in vicinity of the critical angle is presented in Fig. 5.

The difficulty of the fit was connected with a rather smeared hyperfine field distribution, typical for the disordered FeAl alloys (Yelsukov *et al.*, 1992; Voronina *et al.*, 2018), at each depth. This distribution was approximated by 4 multiplets specific for each position on the sample, excluding the case of an unirradiated part of the sample (top row in Fig. 5) where just two resonant singlets were sufficient for acceptable fit. During the fit their depth distribution in 38 steps across the film thickness was obtained. The shape of the total density of ^{57}Fe nuclei was fixed to the depth profile of the electronic density (dashed line above the partial depth profiles for nuclei with selected types of the hyperfine fields in the middle column of Fig. 5). The maximum of this total depth profile was normalized to the expected density of ^{57}Fe atoms in $\text{Fe}_{60}\text{Al}_{40}$ structure taking into account its natural abundance by ^{57}Fe isotope. Due to the obtained depth profile for each multiplet (see the middle column in Fig. 5), their sum gives the total resonant spectrum, characterizing the magnetic hyperfine splitting at each depth (the right column in Fig. 5).

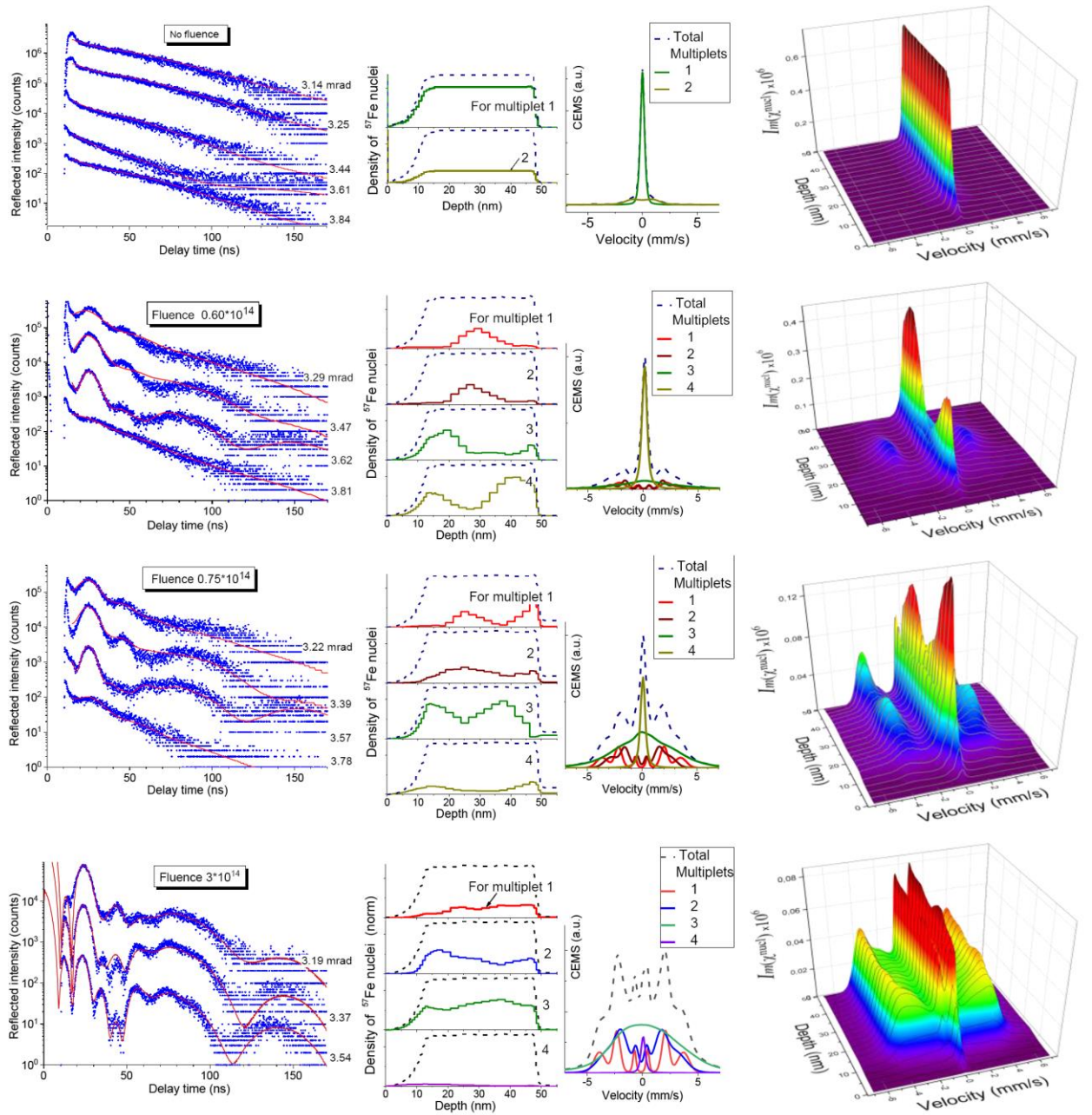


Figure 5

NRR time spectra measured at several grazing angles in the vicinity of the critical one for selected positions on the $Fe_{60}Al_{40}$ gradient sample (left column, symbols are the experimental counts, lines are the fit), the depth distribution of the ^{57}Fe nuclei with selected types of hyperfine interaction and the corresponding resonant spectra for the normal direction of the radiation obtained by the fit (middle column) and overall resonant spectra at each depth $Im(\chi^{nucl}(\omega, z))$ calculated for the direction along the grazing incident SR beam (right column).

The fitting results demonstrate that the relative weight of the magnetically split resonant contributions increases with increasing the irradiation fluence. These findings are in agreement

with the results obtained from XMCD measurements at the Fe K-edge in the paper of La Torre *et al.*, 2018 and by soft X-rays studies (Smekhova *et al.*, submitted).

The essential advantage of the present NRR experiment is that it exposes the depth distribution of different magnetic and paramagnetic fractions inside the irradiated film and their redistribution under the increasing irradiation fluence. As follows from Fig. 5, at the initial stages of the irradiation the ferromagnetic part, giving the mostly split resonant lines (corresponding to magnetic hyperfine fields of $\sim 18 \div 23$ T), appeared not at the surface, but in the center part of the film (second and third rows in Fig. 5). This result obviously follows from the change of the NRR time spectra with the angle variation. At the angles that lower than the critical one, where the penetration depth for the incident radiation is comparable with the thin surface layer, the “magnetic” oscillations are less pronounced than that at the critical angle, where the penetration depth essentially increases.

The calculations performed on the basis of the binary collision approximation with TRIM program (Ziegler *et al.*, 2010) have as well shown that the maximum of the DPA (displacements per atom) depth distribution (Bali *et al.*, 2014) occurs at a certain depth below the surface. It is supposed that atomic displacements produced by the collisions leave a cascade of vacancies and interstitial atoms, as well as more complex clusters of defects and the created disorder is directly connected with magnetization. According to Huffman & Fisher, 1967 the region of moment-bearing atoms has to be large enough to behave ferromagnetically at room temperature, that can be preferable within the film volume. The formation of magnetic inhomogeneities obviously follow from rather broad hyperfine field distribution at each depth, however their morphology is possible to study not by NRR, but by another methods like nuclear or X-ray resonant GISAXS (Erb *et al.*, 2017; Ragulskaya *et al.*, 2019).

The fitting as well shows that ferromagnetic fractions are partially formed at the interface with the SiO₂ substrate (probably due to the imperfections presented near this interface). Some ferromagnetic regions appear to be present at the interfacial region. This may occur due to interfacial inhomogeneities as well as uncertainties in the analysis, discussed later.

With higher fluence (3.0×10^{14} ions/cm²) the depth distribution of the ferromagnetic fractions became more homogeneous across the film (bottom row in Fig. 5). It is better seen in Fig. 6, where the average $\mathbf{B}_{Av}^{hf}(z)$ is presented for three different cases of fluence, corresponded to $\mathbf{B}_j^{hf}(z)$ in Fig. 5. This result more or less coincides with the direct holographic observations in TEM through the measured gradient of the magnetic phase shift (Röder *et al.*, 2015) which shows a practically flat magnetization distribution in Fe₆₀Al₄₀ film after Ne⁺ ions irradiation with even higher fluence (6.0×10^{14} ions/cm²).

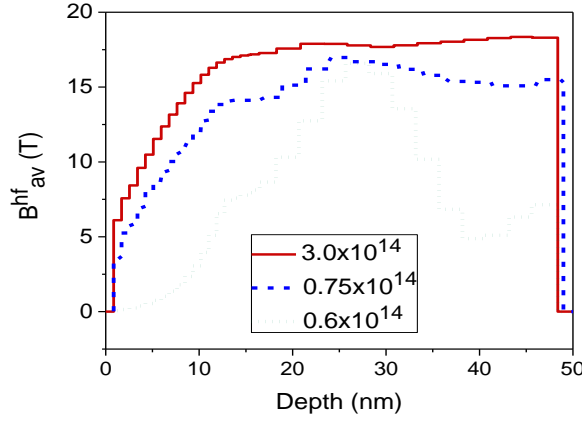


Figure 6

Depth dependence of the average magnetic hyperfine field obtained from the fitting results shown in Fig. 5 for three different irradiation fluences.

The detection of the ferromagnetic fractions at the interface with the SiO₂ substrate is not fully reliable due to the restricted sensitivity of the radiation to that deep part of the film at the used grazing angles. It can be shown that the maximal sensitivity of the method is determined by the radiation field amplitude inside the sample. The nuclear resonant scattering in the studied Fe₆₀Al₄₀ film is essentially smaller than the electronic scattering because the sample is not enriched by ⁵⁷Fe. In such a case the NRR amplitude can be described by the generalized kinematic approximation (Andreeva, *et al.*, 2019). Supposing the σ -polarization of the SR beam, the frequency dependent part of the reflectivity amplitude can be calculated in this approach by the expression

$$R^{\sigma \rightarrow \sigma', \sigma \rightarrow \pi'}(\theta, \omega) = \frac{\pi}{\lambda \sin \theta} \int \chi^{\text{nucl}, \sigma \rightarrow \sigma', \sigma \rightarrow \pi'}(z, \omega) E_{\sigma}^2(\theta, z, \omega) dz, \quad (6)$$

which after Fourier transform gives the NRR time spectra:

$$I(\theta, t) = \left| \frac{1}{2\pi} \int_{-\infty}^{+\infty} R^{\sigma \rightarrow \sigma'}(\theta, \omega) e^{-i\omega t} d\omega \right|^2 + \left| \frac{1}{2\pi} \int_{-\infty}^{+\infty} R^{\sigma \rightarrow \pi'}(\theta, \omega) e^{-i\omega t} d\omega \right|^2. \quad (7)$$

If the nuclear resonant scattering is small enough compared with the scattering by electrons, the calculation of $E_{\sigma}(\theta, z)$ can be done neglecting the nuclear resonance scattering, in other words taking into account only $\chi^{el}(z)$ and by applying the simple Parratt algorithm (Parratt, 1954). Thereafter it is supposed that the $E_{\sigma}(\theta, z)$ distribution inside the sample will be applicable overall the resonant interaction energy region.

The calculated “squared standing wave” distribution $\left|E_{\sigma}^2(\theta, z)\right|^2$ inside our sample as a function of the grazing incidence angle is presented in Fig. 7b. According to (6) it determines the shape of NRR angular curve (Fig. 7a) measured as an integral over the delayed (after prompt SR excitation) reflectivity:

$$I^{NRR}(\theta) = \int_{\varepsilon}^T I(\theta, t) dt. \quad (8)$$

(T is an interval between SR pulses, ε is a small delay excluding the prompt pulse influence).

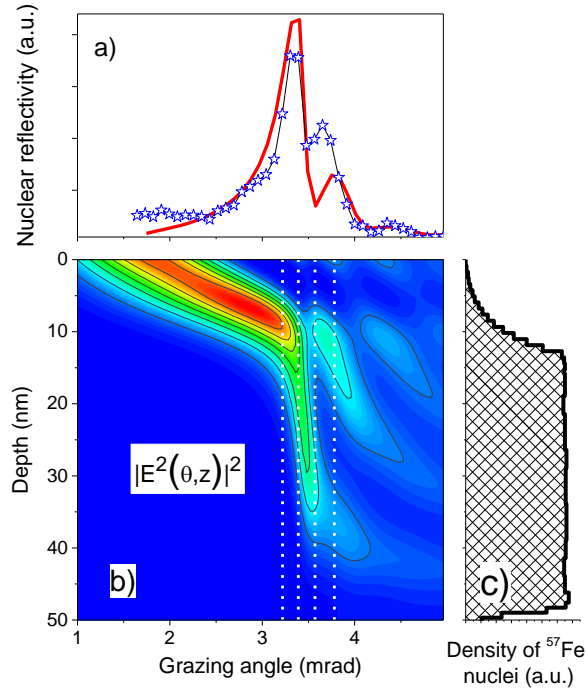


Figure 7

(a) Integrated NRR angular curve $I^{NRR}(\theta)$ measured (symbols) and calculated by (6)-(8) (solid line). (b) The angular-depth distribution of $\left|E_{\sigma}^2(\theta, z)\right|^2$. (c) The depth distribution of the ^{57}Fe nuclei. Calculations for the part of $\text{Fe}_{60}\text{Al}_{40}$ sample irradiated with 0.75×10^{14} ions/cm² fluence (third row in Fig. 5). The function $\left|E_{\sigma}^2(\theta, z)\right|^2$ in (b) is normalized to the amplitude of the incident wave $E_0=1$, the color gradient changes from 0 to 16. The vertical dash lines in (b) mark the angles at which the NRR time spectra (Fig. 5, left column) were measured.

The NRR angular curve is not similar to X-ray reflectivity curve (Baron *et al.*, 1994), it has a sharp maximum at the critical angle. The origin of this peak has been explained by the standing wave influence created by the prompt electronic scattering (Andreeva & Lindgren,

2002; Andreeva & Lindgren, 2005). The standing wave picture in Fig. 7b explains as well why the magnetic quantum beat oscillations on the time spectra are more pronounced at the grazing angle of 3.57 mrad than at 3.78 mrad. The maximum value of $\left|E_{\sigma}^2(\theta, z)\right|^2$ for the last dash line at 3.78 mrad in Fig. 7b compared with the dash line at 3.57 mrad is shifted to the surface where the created magnetization is smaller according to our calculations (depth profiles of magnetically split spectra in the last column of Fig. 5). The amplitude of the $\left|E_{\sigma}^2(\theta, z)\right|^2$ near substrate at the used grazing angles is quite small therefore the nuclear resonant contribution to the total reflectivity from a bottom region of the film is not so essential. Therefore, for more reliable results of magnetization near the $\text{Fe}_{60}\text{Al}_{40}/\text{SiO}_2$ interface, the measurements of the NRR time spectra should be done at larger grazing angles. However, the NRR intensity is maximal near the critical angle and rapidly drops by the angle increasing. Therefore, the measurements at larger angle are difficult especially for our nonenriched sample.

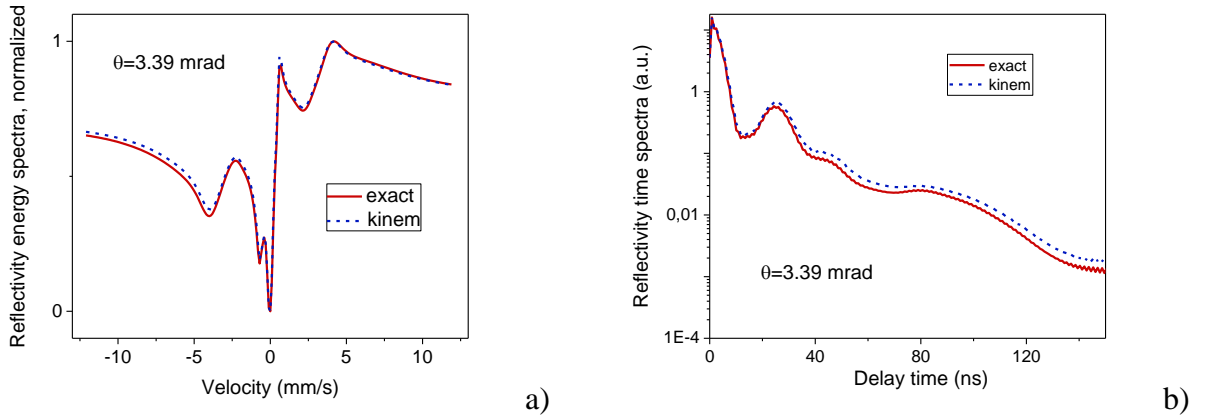


Figure 8

NRR spectra in the energy (a) and time (b) domains calculated at the critical angle of the total reflection for the same sample parameters as in Fig. 5,7 by the exact matrix formalism and by equations (6), (7). The very small difference of the results confirms the validity of the generalized kinematic approximation even in the region of the total reflection and correctness of the depth selectivity interpretation for the used method.

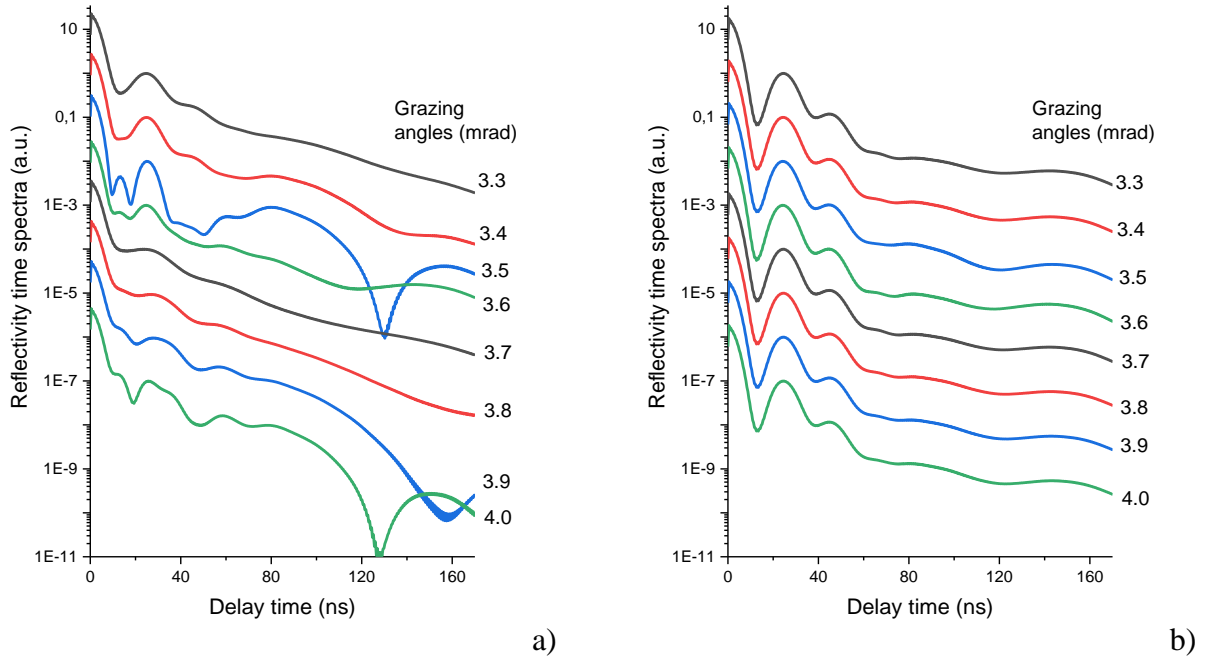


Figure 9

NRR time spectra calculated for several grazing angles for two models of hyperfine field depth-distribution: (a) for the model obtained by fitting of the experimental data at the position irradiated with 0.75×10^{14} ions/cm² fluence and (b) for the case of the same but homogeneously distributed hyperfine fields across the film depth.

The comparison of calculations of the NRR spectra in the energy and time domains by the exact and approximate algorithms shown in Fig. 8 demonstrates that the approach (6), (7) is qualitatively acceptable for the evaluation of the sensitivity of the method. As long as the standing waves influence on the of NRR spectra is proved it should be noted that calculations of the angular-depth distribution of the radiation field inside a film as shown in Fig. 7b are desirable beforehand the experiment, because it helps to determine the right choice of the angles for the NRR spectrum measurements in order to get the real scan of required properties across the film depth. The example of such investigation was recently presented in the paper of Khanderao *et al.* (2020).

In order to exclude that the peculiar shape of the experimental NRR time spectra originated from the specific feature of the reflectivity signal formation but not from the inhomogeneous depth-distribution of the hyperfine fields, the NRR time spectra at several grazing angles for the case of a homogeneous depth distribution were calculated as well. For the homogeneous depth-distribution no essential variations of the NRR time spectra appear. It is easy to see that the remarkable change of the oscillation shapes in Fig. 9a correlates with the brightness of the squared standing waves (Fig. 7b) in the central part of the film, where the magnetic hyperfine fields have the maximal value supposed in the used model (Fig. 5, third row).

The fast variations of the $\left|E_{\sigma}^2(\theta, z)\right|^2$, clearly observable in Fig. 7b, and dramatical variations of the NRR time spectra by very small change of the grazing angle (Fig. 9a) leads to the inference, that NRR experiments need the very accurate adjustment of the angles. If a zero angle is not exactly determined, the information about the depth profiles of the investigated parameters cannot be extracted correctly. In addition, it is important to note that the depth-profile investigations need the measurements of NRR spectra at several grazing angles, but not only at the critical angle (as it is very often practiced). The fit of just one spectrum gives the depth distribution of the hyperfine fields which definitely does not satisfy the other NRR spectra and the obtained result would be rather far from the real model.

4. Summary and conclusions

Initial stages of the ferromagnetic A2 phase formation in the $\text{Fe}_{60}\text{Al}_{40}$ film under 20 keV Ne^+ irradiation with increasing fluence have been investigated by visualizing the depth distribution of hyperfine fields in the film thereby revealing details of the magnetization depth-profiles. The NRR time spectra measured at several grazing angles near the critical angle of the total external reflection evidenced that the highest magnetic hyperfine fields ($\sim 18 \div 23$ T) are initially created in the center part of the film, therefore a formation of the ferromagnetic regions under irradiation does not started from the surface. It is consistent with the fact that a peak in the irradiation induced atomic displacements occurs at a certain distance below the film surface. The results are important for the further development of the computation approaches in modelling phase transformations caused by ion irradiation.

X-ray reflectivity curves measured at different points of the gradually irradiated film with lateral resolution ~ 0.2 mm show a small change in the film thickness (~ 0.5 nm) correlated with the lattice parameter increase and a tiny modification of the top surface layer. Depth-selectivity of the NRR method has been analyzed by application of the standing wave approach. It should be noted that despite the sample was not enriched by ^{57}Fe isotope and contains ^{57}Fe only of natural abundance, the SR based measurements give NRR time spectra of rather good statistics.

Acknowledgements

The authors thank the staff of P01 beamline, PETRA III for the help (proposal I-20160729). A.S. acknowledges Prof. Werner Keune for consultations and Dr. Olaf Leupold for fruitful discussions during the beamtime.

Funding information

H. Wende acknowledge partial support by the DFG (projects No. WE 2623/14-2 and No. BA 5656/1-2). A.S. and C.S.A acknowledge the funding from the Helmholtz Association (VH-NG-1031). A.S. also acknowledges a personal funding from CALIPSO plus project (the Grant Agreement 730872 from the EU Framework Programme for Research and Innovation Horizon 2020).

References

- Andreeva, M. A. & Rosete, C. (1986a). *Vestn. Mosk. Univ. Fiz.* **41**(3), 57.
- Andreeva, M. A. & Rosete, C. (1986b). *Poverkhnost'*, № 9, 145.
- Andreeva M. A. & Lindgren B. (2002). *JETP Letters*, **76**(12), 704.
- Andreeva M.A., & Lindgren B. (2005). *Phys. Rev. B*, **72**, 125422-1.
- Andreeva M.A. (2008). *Hyperfine Interactions* **185**, 17; <http://www.esrf.eu/Instrumentation/software/data-analysis/OurSoftware/REFTIM-1>.
- Andreeva, M., Gupta, A., Sharma, G., Kamali, S., Okada, K. & Yoda, Y. (2015). *Phys. Rev. B* **92**, 134403-1-12. Suppl.: <http://link.aps.org/supplemental/10.1103/PhysRevB.92.134403>.
- Andreeva, M. A., Baulin, R. A., Chumakov, A. I., Ruffer, R., Smirnov, G. V., Babanov, Y. A., Devyaterikov, D. I., Milyaev, M. A., Ponomarev, D. A., Romashev, L. N. & Ustinov, V. V. (2018). *Phys. Rev. B* **97** (2), 024417.
- Andreeva, M.A., Baulin, R.A. & Repchenko, Yu.L. (2019). *J. Synchrotron Rad.* **26**, 483.
- Azzam, R. & Bashara, N. (1977). *Ellipsometry and Polarized Light*. Amsterdam: North-Holland.
- Bali, R., Wintz, S., Meutzner, F., Hübner, R., Boucher, R., Ünal, A.A., Valencia, S., Neudert, A., Potzger, K., Bauch, J., Kronast, F., Facsko, S., Lindner, J. & Fassbender, J. (2014). *Nano Letters* **14**(2), 435–441.
- Baron, A.Q.R., Arthur, J., Ruby, S.L., Chumakov, S.L., Smirnov, G.V., Brown, G.S. (1994). *Phys. Rev. B* **50**, 10354 – 10357.
- Beck, P. A. (1971). *Metallurgical and Materials Transactions B*, **2**(8), 2015–2024.
- Borzdov, G. N., Barkovskii, L. M. & Lavrukovich, V. I. (1976). *Zh. Prikl. Spektrosk.* **25**, 526 (In Russian).
- Diederich, Th., Couet, S., Röhlberger, R. (2007). *Phys. Rev. B* **76**, 054401.
- Ehrler, J., He, M., Shugaev, M. V., Polushkin, N. I., Wintz, S., Liersch, V., Cornelius, S., Hübner, R., Potzger, K., Lindner, J., Fassbender, J., Ünal, A. A., Valencia, S., Kronast, F., Zhigilei, L. V. & Bali, R. (2018). *ACS Applied Materials & Interfaces*, **10**(17), 15232–15239.
- Ehrler, J., Sanyal, B., Grenzer, J., Zhou, Sh., Böttger, R., Eggert, B., Wende, H., Lindner, J., Fassbender, J., Leyens, C., Potzger, K. & Bali, R. (2020). *New J. Phys.* **22**, 073004.

- Erb, D., Schlage, K., Bocklage, L., Hübner, R., Merkel, D. G., Ruffer, R., Wille, H.-C. & Röhlberger R. (2017). *Physical Review Materials* **1**, 023001(R).
- Fassbender, J., & McCord, J. (2008). *J. Magn. Magn. Mater.* **320**(3-4), 579–596.
- Gibert, M., Viret, M., Zubko, P., Jaouen, N., Tonnerre, J.-M., Torres-Pardo, A., Catalano, S., Gloter, A., Sterphan, O. & Triscone, J.-M. (2016). *Nature communications* **7**, 11227.
- Huffman G. P. & Fisher R. M. (1967). *Journal of Applied Physics* **38**, 735.
- Irkaev, S.M., Andreeva, M.A., Semenov, V.G., Belozerskii, G.N. & Grishin, O.V. (1993). *Nuclear Instrum. and Methods in Phys. Res.* **B74**, 554.
- Ishimatsu, N., Hashizume, H., Hamada, S., Hosoi, N., Nelson, C. T., Venkataraman, C. T., Srajer, G. & Lang, J. C. (1999). *Phys. Rev. B* **60**, 9596.
- Jaouen, N., van der Laan, G., Johal, T. K., Wilhelm, F., Rogalev, A., Mylonas, S. & Ortega, S. (2004). *Phys. Rev. B* **70**, 094417.
- Khanderao, A. G., Sergueev, I., Wille, H. C. & Kumar. (2020). *D. Appl. Phys. Lett.* **116**, 101603.
- Liedke, M. O., Anwand, W., Bali, R., Cornelius, S., Butterling, M., Trinh, T. T., Wagner, A., Salamon, S., Walecki, D., Smekhova, A., Wende, H. & Potzger, K. (2015). *Journal of Applied Physics* **117**, 163908.
- Liu, Y., Wang, H.-H., Bian, G., Zhang, Z., Lee, S. S., Fenter, P. A., Tischler, J. Z., Hong, H. & Chiang, T.-C. (2013). *Phys. Rev. Lett.* **110**, 226103.
- Macke, S., Radi, A., Hamann-Borrero, J. E., Verna, A., Bluschke, M., Brück, S., Goering, E., Sutarto, R., He, F., Cristiani, G., Wu, M., Benckiser, E., Habermeier, H.-U., Logvenov, G., Gauquelin, N., Botton, G. A., Kajdos, A. P., Stemmer, S., Sawatzky, G. A., Haverkort, M. W., Keimer, B. & Hinkov, V. (2014). *Advanced Materials*, **26**(38), 6554–6559.
- Menéndez, E., Liedke, M. O., Fassbender, J., Gemming, T., Weber, A., Heyderman, L. J., Rao, K. V., Deevi, S. C., Suriñach, S., Baró, M. D., Sort, J. & Nogués, J. (2009). *Small* **5**(2), 229–234.
- Merkel, D. G., Lengyel, A., Nagy, D. L. Németh, A., Horváth, Z. E., Bogdán, C., Gracheva, M. A., Hegedús, G., Sajti, S., Radnóczy, G. Z. & Szilágyi, E. (2020). *Scientific Reports* **10**:13923.
- Parratt L. G. (1954). *Phys. Rev.* **95**, 359.
- Ragulskaia, A. V., Andreeva, M. A., Rogachev, A. V. & Yakunin, S.N. (2019). *Superlattices and Microstructures* **125**, 16-25.

- Röder, F., Hlawacek, G., Wintz, S., Hübner, R., Bischoff, L., Lichte, H., Kay Potzger, K., Lindner, J., Fassbender, J. & Bali, R. (2015). *Scientific Reports*, **5**(1), 16786.
- Rüffer, R., Gerdau, E., Grote, M., Hollatz, R., Röhlberger, R., Rüter, H.D. & Sturhahn, W. (1991). *Nuclear Instruments and Methods in Physics Research A* **303**, 495.
- Schlage, K., Röhlberger, R., Klein, T., Burkel, E., Strohm, C. & Rüffer, R. (2009). *New Journal of Physics* **11**, 013043.
- Schneider, T., Lenz, K., Semisalova, A., Gollwitzer, J., Heitler-Klevans, J., Potzger, K., Fassbender, J., Lindner, J. & Bali, R. (2019). *J. Appl. Phys.* **125**, 195302.
- Segmüller A. (1973). *Thin Solid Films* **18**(2), 287.
- Smekhova, A., Szyjka, Th., La Torre, E., Ollefs, K., Eggert, B., Cöster, B., Wilhelm, F., Bali, R., Lindner, J., Rogalev, A., Többens, D., Weschke, E., Luo, C., Chen, K., Radu, F., Schmitz-Antoniak, C. & Wende, H., submitted.
- Smirnov, G.V. (1999). *Hyperfine Interactions* **123/124**, 31.
- Tahir, N., Gieniusz, R., Maziewski, A., Bali, R., Potzger, K., Lindner, J. & Fassbender, J. (2015a). *Optics Express* **23**, 16577.
- Tahir, N., Bali, R., Gieniusz, R., Mamica, S., Gollwitzer, J., Schneider, T., Lenz, K., Potzger, K., Lindner, J., Krawczyk, M., Fassbender, J. & Maziewski A. (2015b). *Phys. Rev. B* **92**, 144429-1-7.
- La Torre, E., Smekhova, A., Schmitz-Antoniak, C., Ollefs K., Eggert, B., Cöster, B., Walecki, D., Wilhelm, F., Rogalev, A., Lindner J., Bali, R., Banerjee, R., Sanyal, B. & Wende, H. (2018). *Phys. Rev. B* **98**(2), 024101-1-14.
- Trammell, G.T. (1962). *Phys. Rev.* **126**, 1045.
- Trammell, G.T. & Hannon, J.P. (1978). *Phys. Rev. B* **18**, 165.
- Voronina, E. V., Arzhnikov, A. K., Chumakov, A. I., Chistyakova, N. I., Ivanova, A. G., Pyataev, A. V. & Korolev, A. V. (2018). *Advances in Condensed Matter Physics*, ID 5781873.
- Yelsukov, E. P., Voronina, E. V. & Barinov, V. A. (1992). *Journal of Magnetism and Magnetic Materials* **115**, 271-280.
- Ziegler, J. F., Ziegler, M. D., & Biersack, J. P. (2010). *Nuclear Instruments and Methods in Physics Research Section B: Beam Interactions with Materials and Atoms* **268**(11-12), 1818.